Ibn Al-Haitham Journal for Pure and Applied Sciences
Journal homepage: jih.uobaghdad.edu.iq
PISSN: 1609-4042, EISSN: 2521-3407
IHJPAS. 2026; 39(1)

Magnetic Properties of Nano-Iron Oxide α-Fe_2O_3 Prepared in Green Chemistry from Capsicum Plant Extract

Hassan M.A. Al-Redha[1,2] and **Waleed K. Mahdi**[2*]
[1]Shatrah Education Department, General Directorate of Education in Dhi Qar Governorate, Shatrah, Iraq
[2]Department of Chemistry, College of Education for Pure Science (Ibn Al-Haitham), University of Baghdad, Baghdad, Iraq
*Corresponding Author

Received: 19/July/2025
Accepted: 12/October/2025
Published: 20/ January /2026
doi.org/10.30526/39.1.4253

© 2026. The Author(s). Published by College of Education for Pure Science (Ibn Al-Haitham), University of Baghdad. This is an open-access article distributed under the terms of the Creative Commons Attribution 4.0 International License

Abstract

In this study, iron oxide nanoparticles (α-Fe_2O_3 NPs) were prepared using a readily available chili pepper plant extract from local markets. This study aims to evaluate the magnetic properties of α-Fe_2O_3 prepared in green chemistry from Capsicum plant extract. After several simple preparatory steps, such as washing and cutting, they were treated with an inorganic complex (potassium hexacyanoferrate) ($K_3[Fe(CN)_6]$). In the first analytical step, the *in vitro* detection of the plant extract solution after reaction with the potassium hexacyanoferrate (III) complex revealed characteristic adsorption bands of the cyanide group, which disappeared upon complexation. The iron oxide NPs were characterized using various methods, including X-ray diffraction, energy-dispersive X-ray spectroscopy, scanning electron microscopy, transmission electron microscopy, and atomic force microscopy. The second step, testing the magnetic properties, was conducted using a vibrating sample magnetometer, which revealed strong magnetic properties. This novel method utilizes green chemistry to identify superparamagnetic properties.

Keywords: Green chemistry, Iron oxide, Magnetic properties, Nanoparticles, Plant extract.

1.Introduction

Nanoparticles (NPs) have garnered significant attention in recent years due to their critical applications in electronics, medicine, environmental cleaning, agriculture, and water purification. Magnetic NPs, referred to as nano-adsorbents in ecological applications, have been proposed as a novel solution for the cleanup of seawater contamination resulting from oil spills[1]. Magnetic NPs can be separated from water using an external magnetic field, and their large surface area gives them high adsorption capacity for hydrocarbons. Iron-oxide NPs (IONPs) are widely used magnetic nanomaterials for oil-water separation. They may be surface-functionalized to enhance their capacity for hydrocarbon absorption and/ or increase selectivity for specific contaminants. Furthermore, IONPs are often reusable and can be recovered post-application, thereby reducing overall costs and environmental impacts of the wastewater cleanup process. The use of magnetic IONPs for the separation of oil from water is a promising technique that has been investigated over the past few decades, offering practical and viable options for safeguarding marine ecosystems and coastal populations[2]. Ferric oxides are among the most well-investigated transition metal oxides, exhibiting four polymorphic phases: α-Fe_2O_3 (haematite); β-Fe_2O_3 (magnetite); γ-Fe_2O_3 (maghemite); and ϵ-Fe_2O_3. The β-Fe_2O_3 and ϵ-Fe_2O_3 phases are often synthesized in laboratory settings, but α-Fe_2O_3 and γ-Fe_2O_3 occur naturally. Each polymorph exhibits distinct crystal structures and physical characteristics[3]. Haematite possesses several intriguing qualities, including abundance, low toxicity, environmental friendliness, cost-effective production, chemical inertness, and biocompatibility[4-8]. The characteristics of α-Fe_2O_3 render it a compelling transition metal oxide, prompting vigorous research into its synthesis and applications across various technological domains, including sensors, wastewater treatment, drug delivery, magnetic material coatings, catalysts, magnetic hyperthermia[9], supercapacitors, and cancer therapy[10]. Iron oxide NPs were synthesized using several approaches, including hydrothermal procedures, sol–gel reactions, microwave synthesis, co-precipitation, so no-chemical processes, and microemulsion techniques. Chemical synthesis procedures typically employ toxic substances that can generate hazardous by-products[11]. Subsequently, other green synthesis strategies utilizing plant extracts and other biological materials have been explored[12]. The use of plant extract microorganisms may serve as an environmentally sustainable alternative to traditional techniques for the synthesis of metal or metal oxide NPs. Plant components, such as leaves, seeds, fruits, and root extracts, contain phytochemicals that function as both reducing agents and capping/ stabilizing agents. Consequently, green synthesis techniques for NPs are favored over physical and chemical approaches due to the reduction of toxic chemical solvents and products that pose risks to human health and the environment, as well as for their straightforward, cost-effective nature. In this work, Capsicum annuum was used as the natural source for synthesizing the NPs. Its extract contains compounds of interest due to their chemical composition, such as flavonoids (e.g., lutein and quercetin), capsaicinoids (e.g., capsaicin), terpenoids, and phenolic acids (e.g., vanillic, gallic, and caffeic acid). For this, it is a great candidate for use. Characterization techniques included Scanning electron microscopy (SEM)/ EDS, X-ray diffraction (XRD), and FTIR[13]. In measuring vibration sample magnetometer (VSM) curves, the relationship between the applied magnetic field and the sample's magnetic moment is represented in a graph known as a Hysteresis Loop[14]. The units used depend on the chosen system of units (SI or CGS): In the international system of units (SI), the horizontal axis (applied magnetic field) is measured in amperes per meter (A/m) or tesla (T). Vertical axis (sample magnetic moment): Measured in amperes per square meter (A/m^2) or amperes per kilogram (A/kg) (if specific magnetism is being measured). In the centimeter-gram-second (CGS) system of units, the horizontal axis (applied magnetic field) is measured in ørsted (Oe). Vertical axis (sample magnetic moment): measured in electromagnetic units (emu). Specific magnetism is often expressed in emu/g. Quantity (SI): unit of measurement (CGS): unit of measurement magnetic field (A/m) or T Oe magnetic moment ($A{\bullet}m^2$) or A/kg emu or emu/g. VSM technique can be a valuable tool for detecting the presence of oxygen in a nanometal in the form of a nanometal oxide by measuring changes in the magnetic properties of the sample. However, these results must always be combined with information from other analytical techniques to obtain a complete and accurate picture of the material composition[15]. The VSM curves of nanometals and nanometal oxides can be interpreted by considering their magnetic properties at the nanoscale[16-18]. This study aims to create clean, straightforward, and environmentally friendly processes for NP manufacturing.

2. Materials and Methods

2.1. Materials

Ethyl alcohol (C_2H_5OH, ≥ 99.8%) was purchased from Honeywell (Germany). Sodium hydroxide (NaOH) and sodium borohydride ($NaBH_4$) were obtained from Sigma-Aldrich (USA), and potassium hexacyanoferrate was sourced from Riedel-de Haën (Germany). The solutions were prepared using distilled water and capsicum extract after several preparatory procedures. A digital pH meter was used to measure the pH. All chemicals used were suitable for analysis and of high purity.

2.1.1. Synthesis of iron oxide NPs (α-Fe_2O_3) with capsicum plant extract as a stabilizer

The capsicum extract was obtained after the plant was chopped and washed with water to remove any dirt or impurities. The extract was placed in a volumetric flask, and 250 mL of deionized water was added. The mixture was heated to 50°C under continuous stirring for 30 min, turning orange. The mixture was filtered while hot, and 200 mL of the filtrate was collected. Then, 100 mL of 0.1 M potassium hexacyanoferrate (III) solution, $K_3[Fe(CN)_6]$, a dark red solution, was added in a 1:2 ratio. The solution was heated for 30 min and filtered at 25°C. Then 0.1 M of sodium hydroxide (NaOH) was added, followed by $NaBH_4$ powder, resulting in a blue color with continuous stirring. The precipitate was separated by centrifugation for 10 min at 4000 rpm. After that, it was filtered, and then the precipitate was washed with hot deionized water and hot ethanol. These steps are shown in **Equations 1** and **2** below.

$$K_3[Fe(CN)_6] + 3NaOH \longrightarrow Fe(OH)_3 + 3NaCN + 3KCN \qquad \textbf{(1)}$$

$$2\ Fe(OH)_3 \xrightarrow[NaBH_4]{\Delta} \alpha\text{-}Fe_2O_3 + 3\ H_2O \qquad \textbf{(2)}$$

The precipitate was then allowed to dry for 24 hr and transferred to a dry oven at 400°C for 3 hr. The final precipitate was dark[19] red, as shown in **Figure 1**.

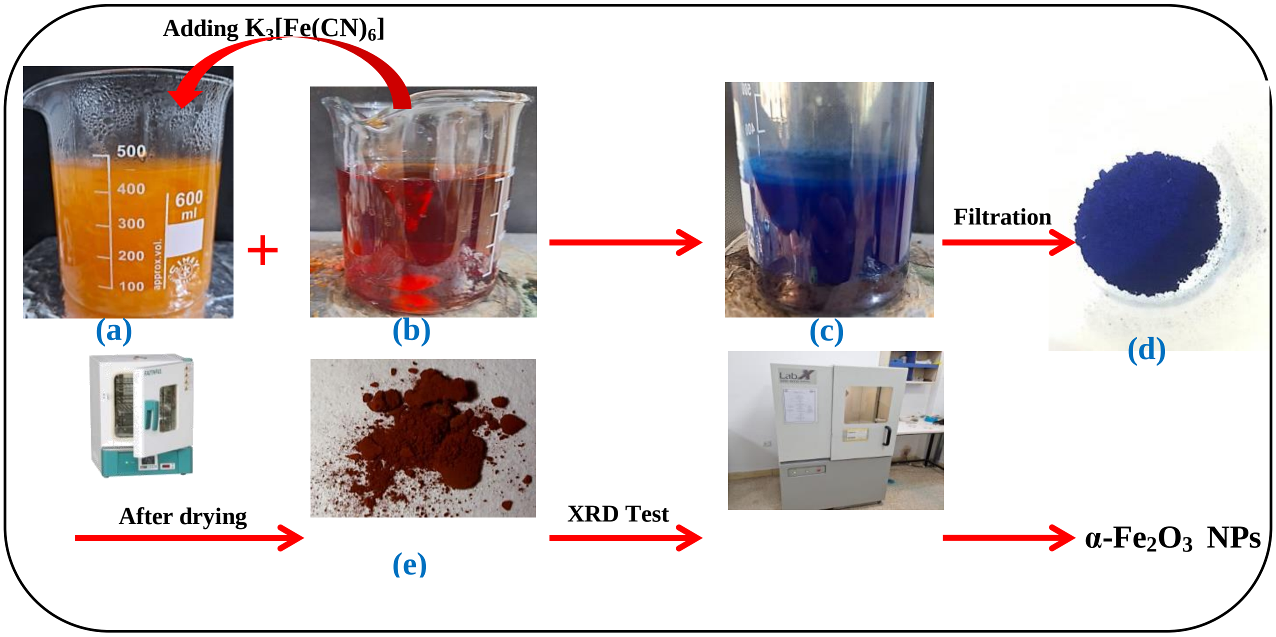

Figure 1. The method for preparing α-Fe_2O_3 NPs involves the main steps from the plant extract to drying the NPs: (a) plant extract, (b) solution of potassium hexacyanoferrate, (c) mix a+b, (d) powder of α-Fe_2O_3 NPs before drying, (e) powder of α-Fe_2O_3 NPs after drying.

3. Results

3.1. FTIR analysis

The infrared spectrum in **Figure 2** for the potassium hexacyanoferrate (III) complex $K_3[Fe(CN)_6]$ of the substrate showed the appearance of a single stretching peak at 2115.77 cm^{-1} due to the cyanide group CN^{-1} attached to the central atom, and the presence of multiple bands at 576.68, 511.10, and 447.45 cm^{-1} due to the components of the plant extract used[20]. **Figure 3** shows the disappearance of the OH band at 3431.13 cm^{-1} and the CN^- band at 2115.77 cm^{-1} after thermal drying at 285 °C, confirming the removal of these groups. New bands at 427.61, 420.44, and 413.26 cm^{-1} indicate the formation of IONPs, corresponding to Fe–O stretching vibrations, while the band near 439 cm^{-1} is attributed to O–Fe–O bending[21].

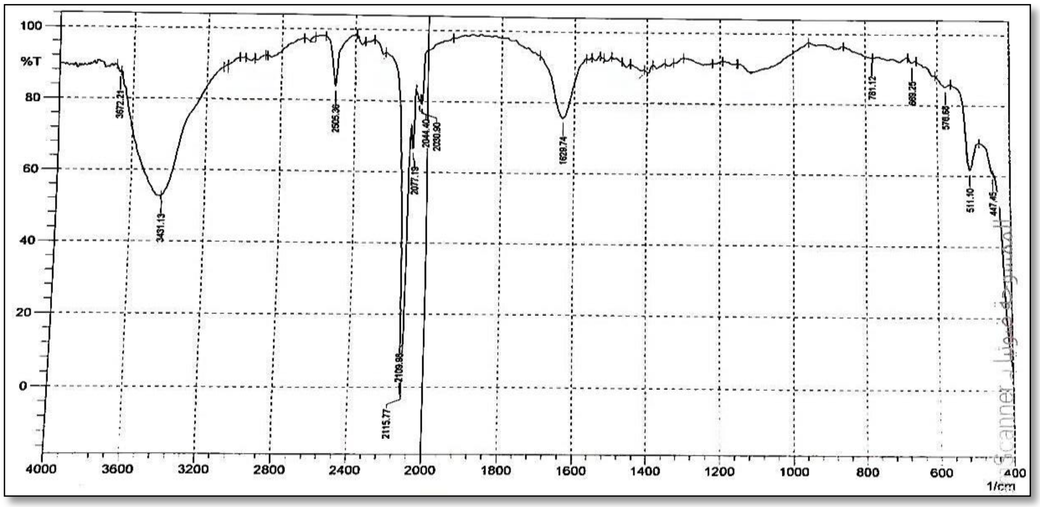

Figure 2. FT-IR analysis of the basic inorganic material potassium hexacyanoferrate (III), $K_3[Fe(CN)_6]$, used in the preparation of nanoparticles before adding it to the plant extract.

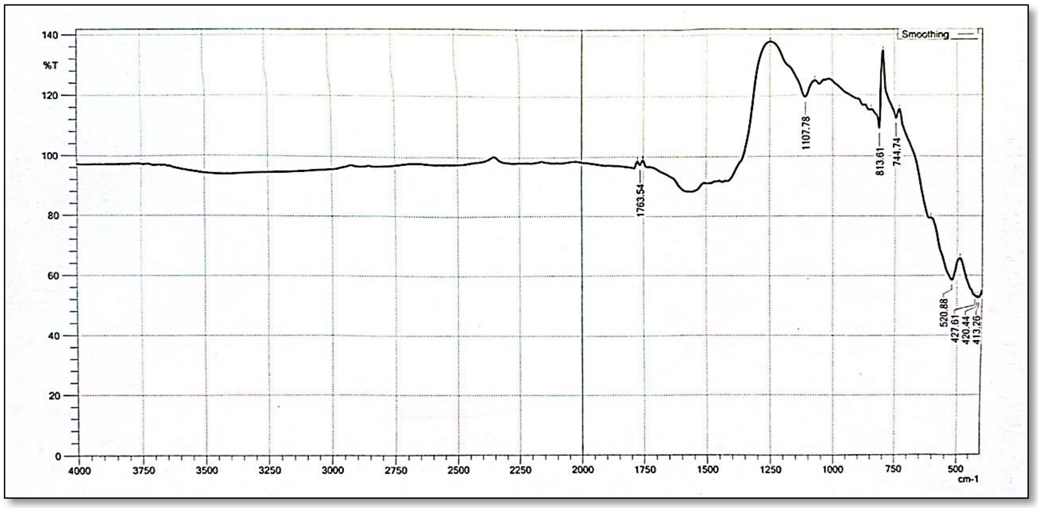

Figure 3. FT-IR analysis of the α-Fe_2O_3 nanomaterial produced by treating the plant extract with the inorganic substance potassium hexacyanoferrate (III) $K_3[Fe(CN)_6]$ after carrying out all preparation methods

3.2. XRD analysis

The average size of the crystals (D) of α-Fe_2O_3 NPs was calculated using the Scherrer equation as presented in **Equation 3** from the XRD image.

$$D = \frac{k\lambda}{\beta \cos\theta} \tag{3}$$

The XRD pattern showed peaks at 24.57°, 33.50°, 35.93°, 42.27°, 43.63°, 49.73°, 54.40°, 57.54°, 62.86, 64.24° and 72.20°, corresponding to the α-Fe_2O_3 miller incidence (012), (104), (110), (113), (202), (024), (116), (122), (214), (300), and (1010), respectively, as shown in **Figure 4**. The analyzed diffraction pattern was matched with the standard XRD peaks of α-Fe_2O_3, as listed in the JCPDS card number. 01–084–0308 and confirmed the formation of hematite phases as shown in **Figure 5**. The optimal parameters were determined based on the minimum particle size (9.59 nm) and the maximum crystallinity (characteristic XRD peaks)[22].

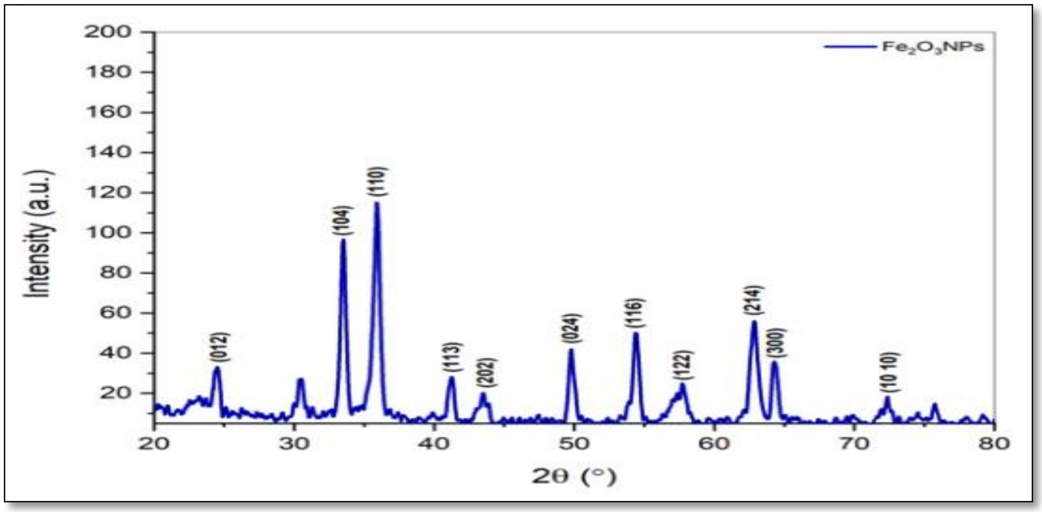

Figure 4. XRD analysis of α-Fe_2O_3 NPs**.**

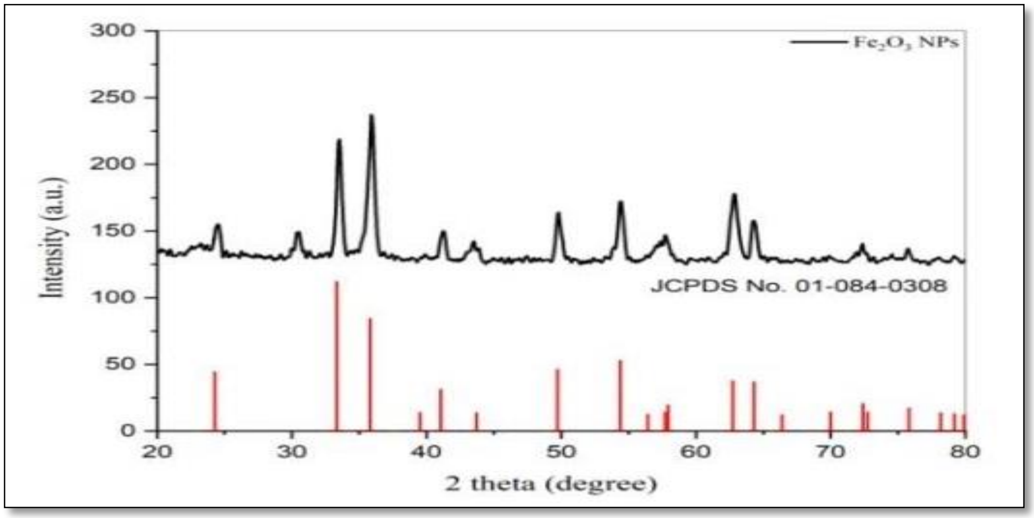

Figure 5. XRD analysis of α-Fe_2O_3 NPs

The crystallite size of the iron oxide NPs was ascertained using the (220) plane corresponding to the peak of highest intensity. The average particle size of the synthesized IONPs is 17.06 nm. The structural properties of the synthesized IONPs were determined using equations derived from XRD data, as shown in **Table 1**.

Table 1. The XRD analysis results of α-Fe_2O_3 NPs

No.	2 theta (degree)	hkl	FWHM (degree)	2 theta (Rad.)	FWHM (Rad.)	D (nm)	Matched by
1	24.5787	012	0.3936	0.214489	0.007	20.649	01-084-0308
2	33.5069	104	0.3149	0.292403	0.005	26.338	
3	35.9372	110	0.4723	0.313611	0.008	17.675	
4	41.2743	113	0.4723	0.360186	0.008	17.966	
5	43.6302	202	0.7872	0.380745	0.014	10.866	
6	49.7312	024	0.4723	0.433987	0.008	18.531	
7	54.4002	116	0.4723	0.474731	0.008	18.904	
8	57.5442	122	0.9446	0.502168	0.016	9.591	
9	62.8661	214	0.551	0.54861	0.010	16.890	
10	64.2407	300	0.4723	0.560606	0.008	19.852	
11	72.209	1010	0.9446	0.630142	0.016	10.405	Average: 17.061

3.3. SEM analysis

The SEM techniques were employed to examine the microstructure and surface characteristics of α-Fe_2O_3 NPs. **Figure 6** shows the SEM micrographs of IONPs, which are agglomerated particles forming large, small, fluffy, and compact NP clusters; the particles are not uniformly dispersed.

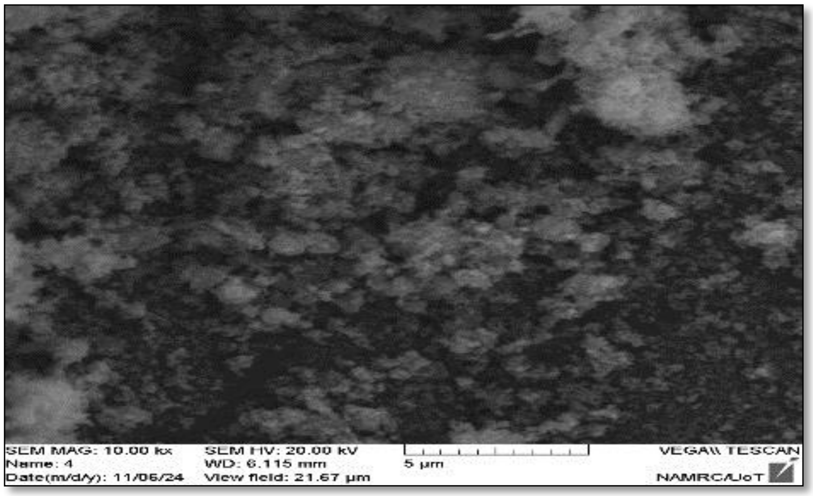

Figure 6. The SEM for α-Fe_2O_3 NPs powder within the range of 5 μm

The image's finer details reveal rough, irregular surfaces, indicating possible NP aggregation and a heterogeneous particle size distribution. Intergranular gaps represent an additional observable characteristic, indicating greater connectivity among grains[23,24].

3.4. Transmission electron microscopy (TEM) analysis

The TEM image in **Figure 7** explains the micrographs of IONPs synthesized by the green chemistry method. In TEM, "Mag= 21.560 KX" indicates a magnification of 21,560 times the original size, using the "Kilo-X" (KX) notation. The "250 nm" specification indicates the scale bar, which represents a length of 250 nanometers on the sample being viewed. These parameters can help in understanding the actual size of features within the magnified image. The prominent characteristic of this image is a rod-like or rectangular structure. The disparity in TEM images is primarily due to differences in electron density[25], indicating a distribution of NPs with a size of 17.06 nm. The imaging software determined particle size from TEM images. The nanoscale synthesis of α-Fe_2O_3 was confirmed via TEM imagery. A narrow distribution of α-Fe_2O_3, with an average particle size of around 17.06 nm, was calculated using Image software. The picture depicts an expanded spread of α-Fe_2O_3. The uniform dispersion of α-Fe_2O_3 is anticipated to enhance catalytic activity. The average particle size was determined from a TEM micrograph[26].

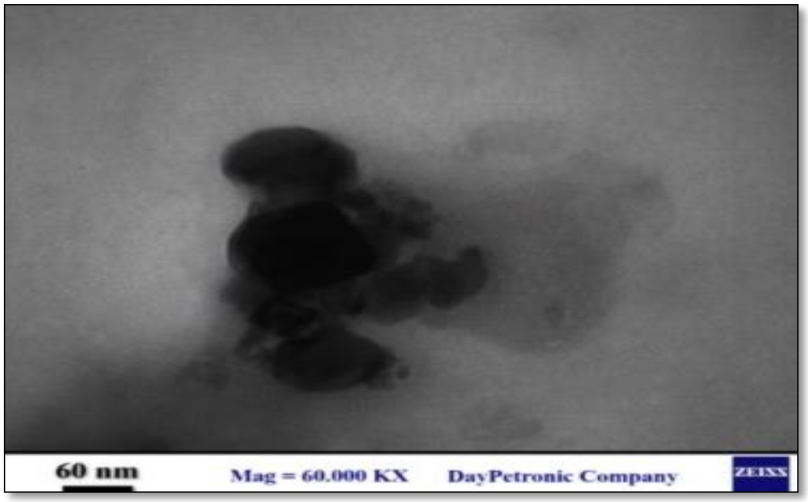

Figure 7. TEM for α-Fe_2O_3 NPs powder within 60 nm

3.5. Energy dispersive X-ray spectroscopy (EDX) analysis

It is a crucial technique for both quantitative and qualitative analysis. It is used to detect the rays emitted from the sample when the electron beam is focused[27]. It identifies the elements present in or on the surface of the sample and measures their analytical composition, as well as their purity in the sample[28]. The electronic image of IONPs, illustrating the SEM-EDX mapping region of the particle, which is likely a NP agglomerate of a mineral cluster. The white box indicates the area selected for elemental analysis using EDX, and the scale bar was 100 µm, indicating the particle is quite large. **Figure 8** shows that the presence of iron oxide in the produced nanostructure was confirmed by EDX spectroscopy, with atomic ratios of 70% iron and 27% oxide. The remaining peaks appearing in the test are due to carbon, hydrogen, and sulfur, which are remnants of the plant extract used. This clearly and precisely demonstrates that the NPs are composed of α-Fe_2O_3[29].

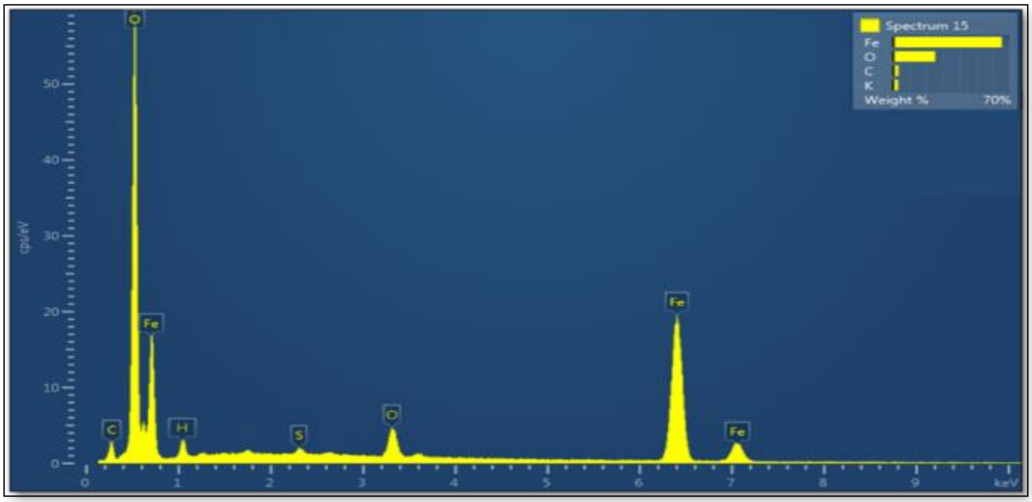

Figure 8. The EDX analysis of α-Fe_2O_3 NPs powder, the peaks illustrate the structure of α-Fe_2O_3.

3.6. Atomic force microscopy (AFM) analysis

This technique is used to examine the size, shape, and structure of nanomaterials, as well as their dispersion and aggregation. **Figures 9**, **10,** and **13** show the AFM particle threshold, histogram, and statistical particle analysis of α-Fe_2O_3 NPs powder. The particle analysis threshold and related information, including specific results with statistics and an image of the particle threshold for iron oxide nanopowder, are presented in **Table 2**.

Table 2. The AFM information and particular results with statistics of α-Fe_2O_3NPs powder**.**

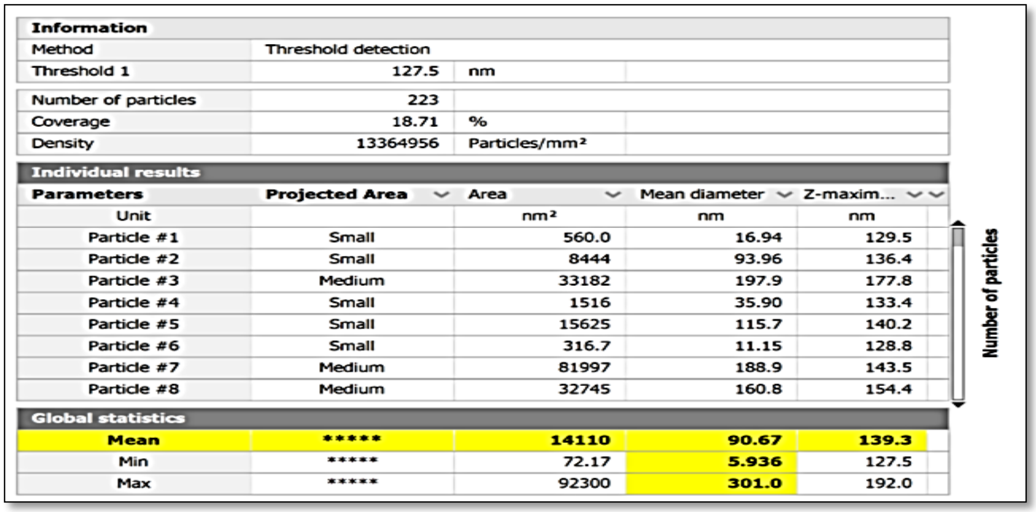

Information				
Method	Threshold detection			
Threshold 1	127.5	nm		
Number of particles	223			
Coverage	18.71	%		
Density	13364956	Particles/mm²		
Individual results				
Parameters	**Projected Area**	Area	Mean diameter	Z-maxim...
Unit		nm²	nm	nm
Particle #1	Small	560.0	16.94	129.5
Particle #2	Small	8444	93.96	136.4
Particle #3	Medium	33182	197.9	177.8
Particle #4	Small	1516	35.90	133.4
Particle #5	Small	15625	115.7	140.2
Particle #6	Small	316.7	11.15	128.8
Particle #7	Medium	81997	188.9	143.5
Particle #8	Medium	32745	160.8	154.4
Global statistics				
Mean	*****	**14110**	**90.67**	**139.3**
Min	*****	72.17	**5.936**	127.5
Max	*****	92300	**301.0**	192.0

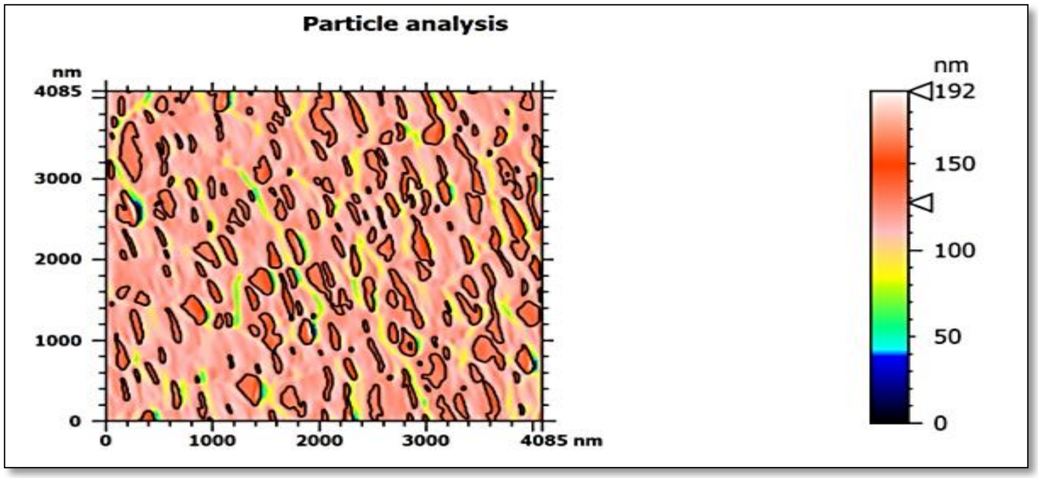

Figure 9. The AFM particle analysis and threshold detection of α-Fe_2O_3 NPs powder.

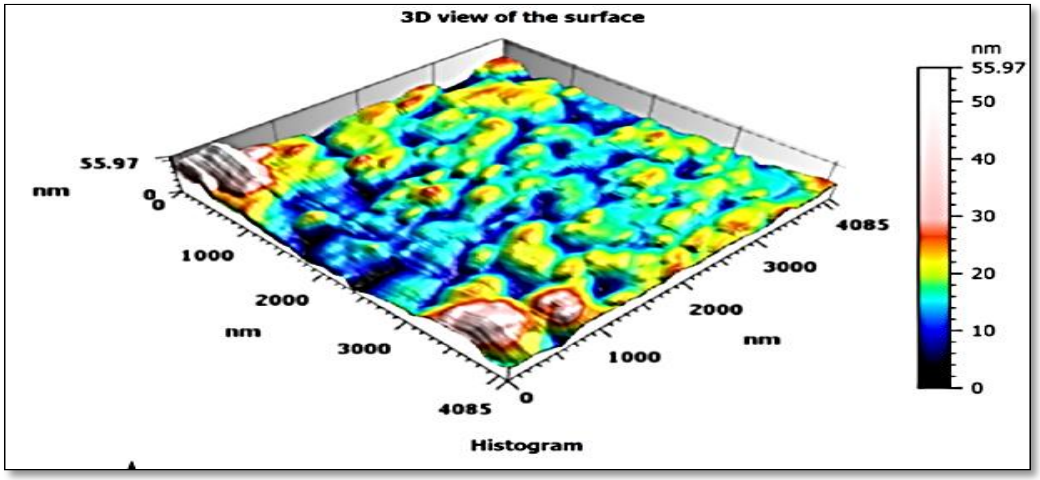

Figure 10. The AFM image of particle threshold of α-Fe_2O_3 NPs powder.

Figures 11 and **12** show the AFM images of roughness (L-S), the primary surface with its topography parameters, and the AFM 3D images of the surface structure of α-Fe_2O_3 NPs powder. The atomic force microscopy images of iron oxide NPs confirm that the particle size falls within the nanorange. The average particle size of the iron oxide, calculated from XRD results, nearly matches the AFM results[30], as shown in **Figure 12**.

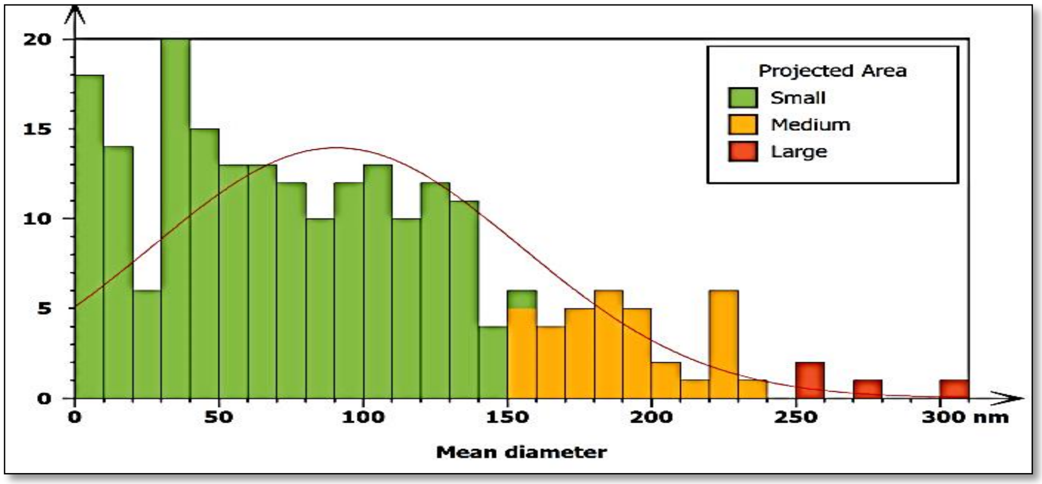

Figure 11. Histogram and statistical particle analysis, the predominant volume fraction of the prepared NPs is clearly visible

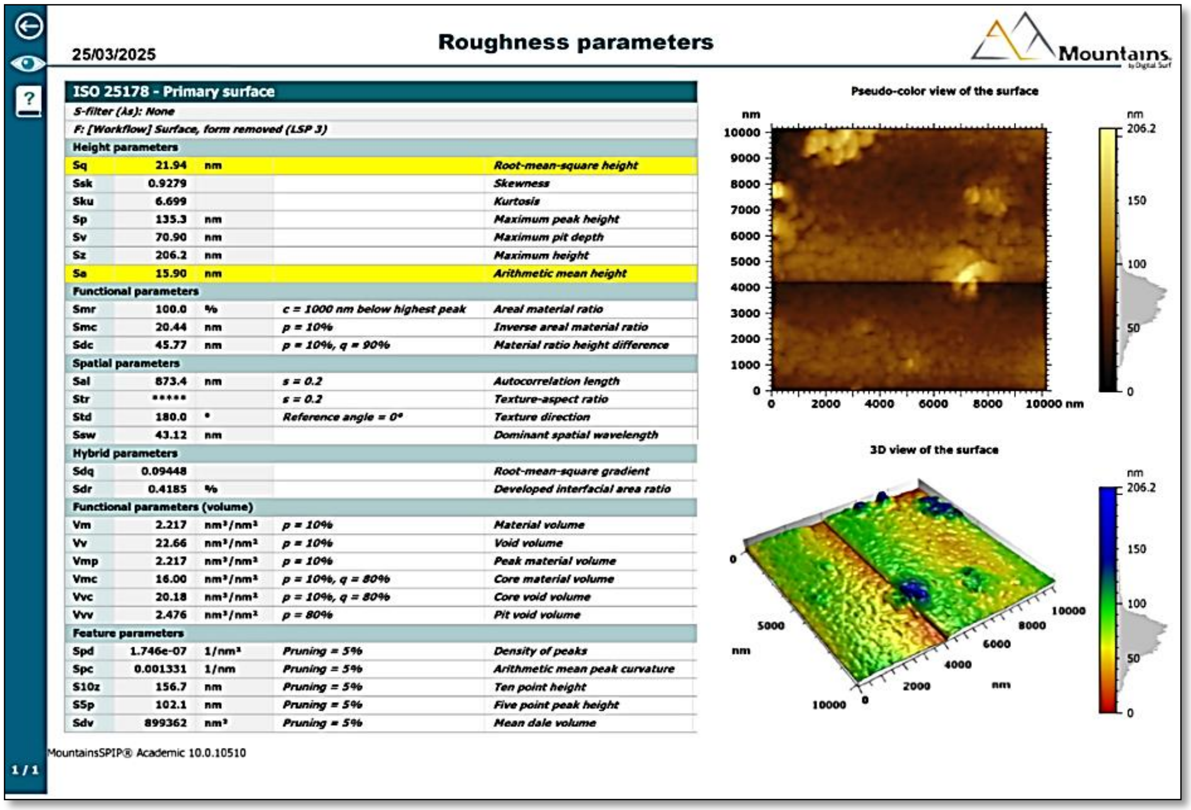

25/03/2025

Roughness parameters

ISO 25178 - Primary surface				
S-filter (λs): None				
F: [Workflow] Surface, form removed (LSP 3)				
Height parameters				
Sq	21.94	nm		*Root-mean-square height*
Ssk	0.9279			*Skewness*
Sku	6.699			*Kurtosis*
Sp	135.3	nm		*Maximum peak height*
Sv	70.90	nm		*Maximum pit depth*
Sz	206.2	nm		*Maximum height*
Sa	15.90	nm		*Arithmetic mean height*
Functional parameters				
Smr	100.0	%	*c = 1000 nm below highest peak*	*Areal material ratio*
Smc	20.44	nm	*p = 10%*	*Inverse areal material ratio*
Sdc	45.77	nm	*p = 10%, q = 90%*	*Material ratio height difference*
Spatial parameters				
Sal	873.4	nm	*s = 0.2*	*Autocorrelation length*
Str	*****		*s = 0.2*	*Texture-aspect ratio*
Std	180.0	°	*Reference angle = 0°*	*Texture direction*
Ssw	43.12	nm		*Dominant spatial wavelength*
Hybrid parameters				
Sdq	0.09448			*Root-mean-square gradient*
Sdr	0.4185	%		*Developed interfacial area ratio*
Functional parameters (volume)				
Vm	2.217	nm^3/nm^2	*p = 10%*	*Material volume*
Vv	22.66	nm^3/nm^2	*p = 10%*	*Void volume*
Vmp	2.217	nm^3/nm^2	*p = 10%*	*Peak material volume*
Vmc	16.00	nm^3/nm^2	*p = 10%, q = 80%*	*Core material volume*
Vvc	20.18	nm^3/nm^2	*p = 10%, q = 80%*	*Core void volume*
Vvv	2.476	nm^3/nm^2	*p = 80%*	*Pit void volume*
Feature parameters				
Spd	1.746e-07	$1/nm^2$	*Pruning = 5%*	*Density of peaks*
Spc	0.001331	1/nm	*Pruning = 5%*	*Arithmetic mean peak curvature*
S10z	156.7	nm	*Pruning = 5%*	*Ten point height*
S5p	102.1	nm	*Pruning = 5%*	*Five point peak height*
Sdv	899362	nm^3	*Pruning = 5%*	*Mean dale volume*

MountainsSPIP® Academic 10.0.10510

Figure 12. AFM images: (Roughness (S-L), and Primary surface) and their topography parameters of α-Fe_2O_3 NPs powder, where the volume percentages of the prepared nanoparticles are shown in colors

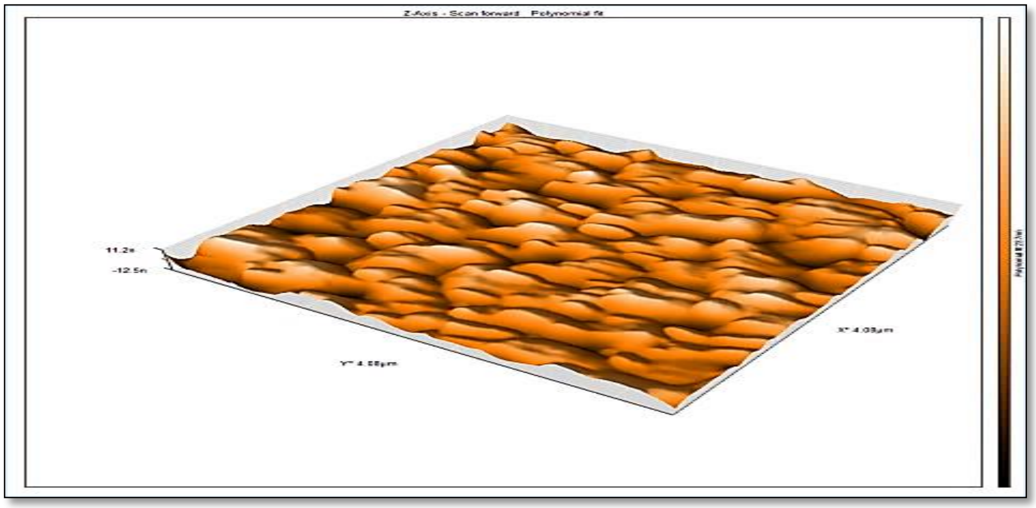

Figure 13. The 3D images of the surface structure of α-Fe_2O_3 NPs powder using AFM

3.7. VSM magnetization study

The VSM test is a widely used method for investigating the magnetic properties of materials. This technique records the magnetic hysteresis loop (M-H loop) under an applied magnetic field and determines parameters such as maximum magnetization (M_{max}), coercivity (Hc), and remanent magnetization (Mr). These parameters provide important information about the nature of magnetic interactions within the material, the magnetic nature of the compound, and structural and electronic variations in the sample. **Figure 14** shows the spectra of the samples under investigation. It shows the extent of the magnetic property of the prepared NPs, and the quantitative results obtained from the test are presented in **Table 3**.

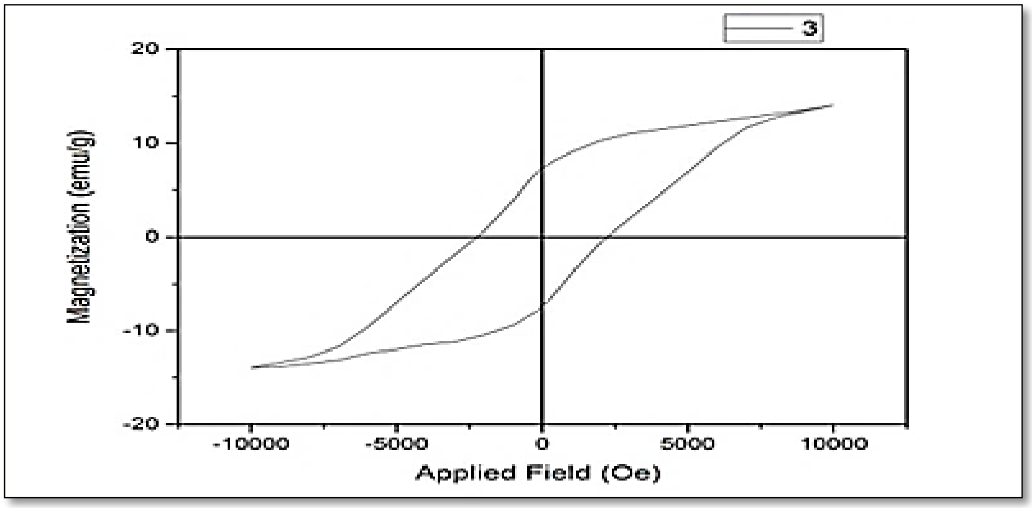

Figure 14. The VSM spectra of the sample under investigation

Table 3. Quantitative results of the Vibrating sample magnetometer (VSM) test for the investigated sample

M_{max} (emu/g)	Hc (Oe)	Mr (emu/g)
14.022	2177.68	7.35

4. Discussion

Nanoparticle size plays a crucial role in determining magnetic properties. Tiny NPs can exhibit superparamagnetic behavior, acting as single magnets with randomly oriented magnetic moments. As particle size increases, ferromagnetic or antiferromagnetic properties may emerge[31]. Structural defects, such as gaps and distortions, can affect magnetic properties. These defects can alter the arrangement of magnetic moments and lead to the formation of different magnetic phases. Temperature affects the magnetic properties of NPs. At low temperatures, quantum effects such as magnetic tunneling may occur. At high temperatures, thermal fluctuations may dominate, leading to superparamagnetic behavior[32]. The composition of nanooxides, including the oxygen content and crystal defects, can influence their magnetic properties[33]. Some nanooxides may exhibit ferromagnetic or antiferromagnetic behavior, while others exhibit superparamagnetic behavior[34].

Magnetic materials exhibit various characteristics, including ferromagnetism, antiferromagnetism, and ferrimagnetism. In some cases, the compounds exhibit canted antiferromagnetic behavior, a combination of antiferromagnetic interactions and a slight degree of ferromagnetic ordering. This phenomenon is typically attributed to super-exchange interactions between metal ions, double-exchange interactions, and the presence of oxygen vacancies[35,36]. Based on the VSM data, the samples exhibit complex magnetic behavior, suggesting the coexistence of antiferromagnetic interactions and a small amount of ferromagnetic order. As shown in **Figure 14**, the magnetization in these samples does not saturate even at an applied field of 10,000 Oe, and it continues to increase with field strength. Therefore, it is more appropriate to use the term M_{max} rather than "saturation magnetization" for comparing samples. According to **Table 3**, the M_{max} values range from 9.336 to 14.078 emu/g. This variation in M_{max} can be attributed to the following factors: a) chemical composition and Fe^{3}/ Fe ratio: An increase in Fe ions can enhance the Fe^{3}-O-Fe double-exchange interactions, resulting in higher M_{max}. b) Oxygen vacancies: Samples with more oxygen vacancies likely have stronger ferromagnetic interactions, contributing to increased M_{max}. Among the values, the sample (14.022 emu/g) exhibits the highest M_{max} values, suggesting stronger Fe^{3}-O-Fe double-exchange interactions. Coercivity (Hc) is a key parameter that indicates a material's resistance to changes in magnetization direction. This may be due to a greater number of oxygen vacancies, which reduce magnetic interactions and enhance superparamagnetic behavior. The high Hc value suggests the sample exhibits more challenging magnetic behavior. The increased Hc could be due to stronger antiferromagnetic interactions, higher structural defect density, and changes in the Fe-O-Fe bond angle. In general, higher Hc typically reflects stronger antiferromagnetic interactions and a reduction in the effects of double exchange, resulting in a greater magnetic field requirement to alter magnetic orientation[37]. Remanent magnetization (Mr) represents the amount of magnetization retained by a material after the external magnetic field is removed. The reduction of Mr in the sample may result from increased Fe^3-O-Fe^3 and Fe-O-Fe super-exchange interactions, which weaken ferromagnetic behavior. Therefore, the VSM test results indicate that the sample exhibits a combination of antiferromagnetic behavior with a slight degree of ferromagnetic ordering, resulting from Fe^3-O-Fe double exchange and Fe^3-O-Fe^3/ Fe-O-Fe super-exchange interactions. The sample demonstrates the highest M_{max} values, reflecting stronger ferromagnetic interactions. Moreover, the sample exhibits the highest coercivity values (Hc), indicating enhanced antiferromagnetic interactions and reduced double-exchange effects. Consequently, the sample, due to its high M_{max} and Mr values, and the sample in particular, due to its high coercivity, exhibit superior magnetic properties compared to other NPs and may be of interest for magnetic applications.

5. Conclusion

This study successfully synthesized and characterized IONPs using Capsicum plant extract as a green reducing and stabilizing agent. FTIR, XRD, SEM, TEM, AFM, and EDX analyses confirmed the formation of well-crystallized NPs (α-Fe_2O_3) with an average size of 17 nm, exhibiting good dispersion with some degree of aggregation. The presence of elements such as C, K, and S indicates the presence of plant extract. Magnetic measurements using a VSM revealed a combination of antiferromagnetic and weak ferromagnetic behavior, characterized by high values of saturation magnetization and coercivity, indicating enhanced magnetic properties. These features make the NPs promising for applications such as drug delivery, catalysis, and adsorption. The use of chili pepper extract offers a rapid, safe, and eco-friendly synthesis route.

Acknowledgment

The authors thank the Department of Chemistry at the College of Education for Pure Science (Ibn Al-Haitham), University of Baghdad.

Conflict of Interest

The authors declare that they have no conflicts of interest.

Funding

There is no financial support for the submitted work.

Ethical Clearance

The guidelines and instructions of postgraduate studies at Baghdad University were followed.

References

1. Mehmood A, Khan FSA, Mubarak NM, Mazari SA, Jatoi AS, Khalid M, Tan YH, Karri RR, Walvekar R, Abdullah EC, Nizamuddin S, Mazari SA. Carbon and polymer-based magnetic nanocomposites for oil-spill remediation—A comprehensive review. Environ Sci Pollut Res. 2021; 28(39):54477–54496. https://doi.org/10.1007/s11356-021-12589-3.
2. Zhang J, Shao Y, Hsieh CT, Chen YF, Su TC, Hsu JP, Juang RS. Synthesis of magnetic iron oxide nanoparticles onto fluorinated carbon fabrics for contaminant removal and oil-water separation. Sep Purif Technol. 2017; 174:312–319. http://dx.doi.org/10.1016/j.seppur.2016.11.006.
3. Singh B, Kumar S, Kishore B, Narayanan TN. Magnetic scaffolds in oil spill applications. Environ Sci Water Res Technol. 2020; 6:436–463. https://doi.org/10.1039/C9EW00697D.

4. Mohamed AF, Mohamed AS, Abdel-Khalek AA, Badran SR. Synergistic impact of temperature rises and ferric oxide nanoparticles on biochemical and oxidative stress biomarkers in Oreochromis niloticus: relevant environmental risk assessment under predicted global warming. Environ Monit Assess. 2025; 197(4):409. https://doi.org/10.1007/s10661-025-13789-x.
5. Sabouri Z, Sabouri S, Tabrizi Hafez Moghaddas SS, Mostafapour A, Amiri MS, Darroudi M. Facile green synthesis of Ag-doped ZnO/CaO nanocomposites with Caccinia macranthera seed extract and assessment of their cytotoxicity, antibacterial, and photocatalytic activity. Bioprocess Biosyst Eng. 2022; 45(11):1799–1809. https://doi.org/10.1007/s00449-022-02786-w.
6. Ashraf M, Khan I, Usman M, Khan A, Shah SS, Khan AZ, Saeed K, Yaseen M, Ehsan MF, Tahir MN, Ullah N. Hematite and magnetite nanostructures for green and sustainable energy harnessing and environmental pollution control: A review. Chem Res Toxicol. 2019; 33(6):1292-1311. https://doi.org/10.1021/acs.chemrestox.9b00308.
7. Asha A, Chamundeeswari M, Flora RM, Preethy KR. Optimization of hematite nanoparticles from natural ore as novel imaging agents: A green chemistry approach. Biotechnol Appl Biochem. 2024; 71(4):791-808. https://doi.org/10.1002/bab.2577.
8. Lemine OM, Madkhali N, Hjiri M, Abdel All N, Aida MS. Comparative heating efficiency of hematite (α-Fe_2O_3) and nickel ferrite nanoparticles for magnetic hyperthermia application. Ceramics International. 2020; 46(18 Part A):28821–28827. https://doi.org/10.1016/j.ceramint.2020.08.047.
9. Mohammed MN, Abdullah OI, Jweeg MJ, Aljibori HS, Abdullah TA, Alawi NM, Rasheed RT, Meharban F, Hamzah HT, Al-Obaidi Q. Comprehensive review on wastewater treatment using nanoparticles: Synthesis of iron oxide magnetic nanoparticles, publication trends via bibliometric analysis, applications, enhanced support strategies, and future perspectives. AJSE. 2025; 5(1):1-30. https://doi.org/10.17509/ajse.v5i1.79487.
10. Khan I, Morishita S, Higashinaka R, Matsuda TD, Aoki Y, Kuzmann E, Homonnay Z, Katalin S, Pavić L, Kubuki S. Synthesis, characterization and magnetic properties of ϵ-Fe_2O_3 nanoparticles prepared by sol-gel method. J Magn Magn Mater. 2021; 538:168264. https://doi.org/10.1016/j.jmmm.2021.168264.
11. Joy J, George N, Wilson R. Chemical synthesis versus green synthesis. In nanomaterial green synthesis. Cham: Springer Nature Switzerland; 2025, Vol. 2, p. 483-512. https://doi.org/10.1007/978-3-031-84643-4_16
12. Lassoued A. Synthesis and characterization of Zn-doped α-Fe_2O_3 nanoparticles with enhanced photocatalytic activities. J Mol Struct.2021; 1239:130489. https://doi.org/10.1016/j.molstruc.2021.130489.
13. Yadav VK, Ali D, Khan SH, Gnanamoorthy G, Choudhary N, Yadav KK, Thai VN, Hussain SA, Manhrdas S. Synthesis and characterization of amorphous iron oxide nanoparticles by the sonochemical method and their application for the remediation of heavy metals from wastewater. Nanomaterials (Basel). 2020; 10(8):1551. https://doi.org/10.3390/nano10081551.
14. Lebedev AV. Measuring magnetization curves of ferrofluids: Comparison of the differential sweep method and a vibrating-sample magnetometer. Instrum Exp Tech. 2024; 67(5):989–994. https://doi.org/10.1134/S0020441224701574.
15. Al-Salman HNK, Ali ET, Jabir M, Sulaiman GM, Al-Jadaan SA. 2-Benzhydrylsulfinyl N-hydroxyacetamide-Na extracted from fig as a novel cytotoxic and apoptosis inducer in A549 and AMJ-13 cell lines via P53 and caspase-8 pathway. Eur Food Res Technol. 2020; 246(8):1-18. https://doi.org/10.1007/s00217-020-03515-x.
16. Shlaka WA, Saeed RS, Negim E. Synthesis and study medical application of nanocomposites based on grafted chitosan /polyvinyl alcohol. IHJPAS. 2024; 37(1):236-250. https://doi.org/10.30526/37.1.3327.
17. Jasim AJ, Sulaiman GM, Ay H, Mohammed SA, Mohammed HA, Jabir MS, Khan RA. Preliminary trials of the gold nanopartifcles conjugated chrysin: An assessment of anti-oxidant, anti-microbial, and in vitro cytotoxic activities of a nanoformulated flavonoid. Nanotechnol Rev. 2022; 11(1):2726-2741. https://doi.org/10.1515/ntrev-2022-0153.
18. Soni RA, Rizwan MA, Singh S. Opportunities and potential of green chemistry in nanotechnology. Nanotechnol Environ Eng.2022;7:661-673.https://doi.org/10.1007/s41204-022-00233-5.

19. Khalaf MM, Gouda M, Abou Taleb MF, Al-Rasheed FE, Abd El-Lateef HM. Bioinspired synthesis of Fe_2O_3 nanoparticles uing Rosa Rugosa flower extract and their application as a potent alternative disinfecting agent against waterborne pathogens within wastewater management. J Taiwan Inst Chem Eng. 2025; 171:106079. https://doi.org/10.1016/j.jtice.2025.106079.
20. Shehu Z, Nyakairu GWA, Tebandeke E, Odume ON. Circular economy approach for treatment of water-containing diclofenac using recyclable magnetic FeO nanoparticles: A case study of real water sample from lake Victoria. J Pharm Res Int. 2023; 35(22):66–81. https://doi.org/10.9734/jpri/2023/v35i227417.
21. Mohamed HEA, Afridi S, Khalil AT, Ali M, Zohra T, Salman M, Ikram A, Shinwari ZK, Maaza M. Bio-redox potential of Hyphaene thebaica in bio-fabrication of ultrafine maghemite phase iron oxide nanoparticles (Fe_2O_3 NPs) for therapeutic applications. Mater Sci Eng C Mater Biol Appl. 2020; 112: 110890. https://doi.org/10.1016/j.msec.2020.110890.
22. Maji SK, Mukherjee N, Mondal A, Adhikary B. Synthesis, characterization and photocatalytic activity of α-Fe_2O_3 nanoparticles. Polyhedron. 2012; 33(1):145-149. https://doi.org/10.1016/j.poly.2011.11.017.
23. Endres TH, Yimer AA,Beyene TT, Muleta GG. An efficient green synthesis of Ag/Fe2O3 nanocomposite using Carica papaya peel extract for enhanced photocatalytic, antioxidant, and antibacterial activities. Results Chem. 2025; 15:102184. https://doi.org/10.1016/j.rechem.2025.102184.
24. Ural N. The significance of scanning electron microscopy (SEM) analysis on the microstructure of improved clay: An overview. Open Geosci. 2021; 13(1):197-218. https://doi.org/10.1515/geo-2020-0145.
25. Saeed RS, Hassan HA, Hassan DF, AL-Rawi MS. Modification and study biological activity of chitosan with compounds containing azo group. Baghdad Sci J. 2025; 22(2):428-437. https://doi.org/10.21123/ bsj.2024.9453.
26. Morshedy AS, Mahmoud T. Optimizing heavy crude oil conversion: Catalytic thermolysis with TiO_2@ α-Fe_2O_3 nanocomposite and surfactant dynamics. Petroleum. 2025; 11:234-247. https://doi.org/10.1016/j.petlm.2025.02.003.
27. Mouhamad RS, Al Khafaji KA, Al-Dharob MH, Al-Abodi EE. Antifungal, antibacterial and anti-yeast activities evaluation of nanoparticles. Chem Int. 2022; 8(4):159-166. https://doi.org/10.5281/zenodo.7317423.
28. Ali EH, Naser JA, Ahmed ZW, Himdan TA. Corrosion protection of 5083 AA in saline water by polyacrylonitrile nanofibers. J Renew Mater. 2021; 9(11):1927-1939. https://doi.org/10.32604/jrm.2021.015624.
29. Flayyih AO, Mahdi WK, Abu Zaid YIM, Musa FH. Biosynthesis, characterization, and applications of bismuth oxide nanoparticles using aqueous extract of beta vulgaris. Chem Methodol. 2022; 6(8): 620-628. https://doi.org/10.22034/CHEMM.2022.342124.1522.
30. Shukla V. Introduction of vibrating sample magnetometer for magnetic characterization. In: Thomas S, Rezazadeh Nochehdehi, A. (eds) Handbook of Magnetic Hybrid Nanoalloys and their Nanocomposites. Springer, Cham. 2022. https://doi.org/10.1007/978-3-030-90948-2.
31. Bohra M, Giaremis S, Abisegapriyan KS, Mathioudaki S, Kioseoglou J, Grammatikopoulos P. Ferromagnetic–antiferromagnetic coupling in gas-phase synthesized M (Fe, Co, and Ni)–Cr nanoparticles for next-generation magnetic applications. Adv Sci. 2024; 11(43):2403708. https://doi.org/10.1002/advs.202403708.
32. Phillips J, Yazdani S, Highland W, Cheng R. A high sensitivity custom-built vibrating sample magnetometer. Magnetochemistry. 2022; 8(8):84. https://doi.org/10.3390/magnetochemistry8080084.
33. Ibrahim AA, Kareem MM, Al-Noor TH, Al-Muhimeed T, AlObaid AA, Albukhaty S, Sahib UI. Pt (II)-Thiocarbohydrazone complex as cytotoxic agent and apoptosis inducer in Caov-3 and HT-29 cells through the P53 and Caspase-8 pathways. Pharmaceuticals. 2021;14(6):509. https://doi.org/10.3390/ph14060509.
34. Al-Rawi MA, Hassan GM, Fahad HM. The latest studies for the manufacture of nanoparticles in Iraq during the last ten years ago. Haya Saudi J Life Sci. 2024; 9(4):79-87. https://doi.org/10.36348/sjls.2024.v09i04.001.

35. Abdel-Khalek EK, Alluhayb AH, Younis AM, Mohamed EA. Study the influence of Ag^+ nanoparticles on the surface of the Sr1-xAgxFeO_3- perovskite on optical, magnetic and antibacterial properties. J Sol-Gel Sci Technol. 2024; 112:44-58. https://doi.org/10.1007/s10971-024-06487-6.
36. Kadhim RJ, Karsh EH, Taqi ZJ, Jabir MS. Biocompatibility of gold nanoparticles: In-vitro and In-vivo study. Mater Today Proc. 2021; 42(Part 5):3041-3045. https://doi.org/10.1016/j.matpr.2020.12.826,
37. Chen JB, Ying J, Tian Y, Xiao YX, Yang XY. Electrocatalysis under magnetic fields. Adv Funct Mater. 2025; 35(8):2415660. https://doi.org/10.1002/adfm.202415660.